

Article

Acousto-Optic Transfer Function Control by a Phased-Array Piezoelectric Transducer

Konstantin B. Yushkov * , Alexander I. Chizhikov and Vladimir Ya. Molchanov

Acousto-Optical Research Center, University of Science and Technology MISIS, Moscow 119049, Russia; chizhikov.ai@misis.ru (A.I.C.); v.ya.molchanov@gmail.com (V.Y.M.)

* Correspondence: konstantin.yushkov@misis.ru

Abstract: We present analysis and numerical simulations of the acousto-optic spatial filter (AOSF) transfer function under the condition of dual-transducer operation and phase control. Based on these simulations, the AOSF crystal configuration is optimized for operation in the near-infrared wavelength region from 0.7 to 1.0 μm . We demonstrate that ultrasonic phase control can provide efficient tuning of the transfer function, which is independent of conventional frequency control. Thus, the application of phase control coupled with frequency control can reduce the transfer function asymmetry that is inherent to anisotropic Bragg diffraction in uniaxial crystals.

Keywords: acousto-optic tunable filter; laser beam shaping; ultrasound; beam steering

1. Introduction

The field of laser beam shaping (LBS) includes various methods for the transformation of the spatial profile of a single beam into a desired spatial distribution [1]. These methods can be grouped as passive and active ones. The former group includes transformations of the spatial distribution by means of refractive or diffractive optical elements: aspherical lenses, polarizers, metasurfaces, etc. The second group includes optical schemes based on programmable photonic elements: spatial light modulators (SLMs) including liquid-crystal, micro-electro-mechanical and acousto-optic (AO) devices. The scope of problems LBS can address includes both the static and dynamic generation of arbitrary spatial distributions.

LBS is one of the emerging applications of acousto-optic (AO) tunable filters (AOTFs) [2,3]. AOTFs directly filter the angular spectrum of laser beams, as first shown by Balakshy [4]. Based on special phase-matching conditions in birefringent crystals, acousto-optic spatial filters (AOSFs) can provide a variety of transfer functions [5–9]. There are several fundamental topologies of an AOSF's transfer function, which are determined by the curvature tensor of the optical wave normal surface [10]. In particular, the annular topology of the transfer function is typical for noncollinear AOTFs in uniaxial birefringent crystals. This is the most common AOTF type, widely available and used in various hyperspectral imaging experiments [11,12]. Several previous applications of AO devices for optical image processing include image edge enhancement in coherent light [13–20] and phase imaging [21–23]. Novel designs of optical traps based on LBS by an AOSF have been recently demonstrated by Obydenov et al. [24,25]. These results include annular particle trapping [24] and multicolor bottle beam generation [25]. Apart from AOTFs, LBS can be obtained with the help of programmable acousto-optic modulators and deflectors. A number of AO systems have been proposed for the design of laser-based displays and image projectors [26–29]. Antonov et al. [30,31] studied multi-beam diffraction of a laser beam in a single Bragg cell both theoretically and experimentally and demonstrated precisely controllable splitting of a single beam into five output beams. Trypogeorgos et al. [32] demonstrated one-dimensional LBS with a deflector operating in a multifrequency regime. Szulzycki et al. [33,34] developed an AO lens and demonstrated its application for image edge enhancement. Karimi et al. [35] developed an AO light modulator having a cylindrical



Citation: Yushkov, K.B.; Chizhikov, A.I.; Molchanov, V.Y. Acousto-Optic Transfer Function Control by a Phased-Array Piezoelectric Transducer. *Photonics* **2023**, *10*, 1167. <https://doi.org/10.3390/photonics10101167>

Received: 4 September 2023

Revised: 16 September 2023

Accepted: 17 October 2023

Published: 19 October 2023



Copyright: © 2023 by the authors. Licensee MDPI, Basel, Switzerland. This article is an open access article distributed under the terms and conditions of the Creative Commons Attribution (CC BY) license (<https://creativecommons.org/licenses/by/4.0/>).

geometry of diffraction of light by low-frequency standing waves in water for the generation of dipole and quadrupole beams. Bola et al. [36] applied AO digital holography for creating a multi-spot optical trap with a two-dimensional configuration. This demonstrates a variety of AO techniques for LBS applications.

The operation principle of an AOSF is based on anisotropic diffraction in a birefringent crystal [37,38], and the transfer function is defined both by the bulk acoustic wave (BAW) propagation direction and the ultrasound frequency [39]. Yushkov et al. [9,10] demonstrated that under the noncritical phase matching (NPM) condition in a birefringent crystal, there are two stable transfer function configurations having X-type and O-type topologies. Both these configurations provide a wide acceptance angle of Bragg diffraction and are used in different AOTF designs: X-type topology takes place in collinear AOTFs and O-type topology takes place in noncollinear AOTFs. Intermediate points correspond to topological transitions and take place only in special directions of AO interactions in a crystal. The principal difference between AO SLMs and AOSFs is that the former use a spatially modulated ultrasound to create a digital hologram in the AO interaction region, while the latter directly modulate the angular spectrum of the laser beam. The maximum operation rate of an AOSF is limited by the acoustic wave transit time across the laser beam, which is typically on the order of a few microseconds [40]. Thus, AOSFs have a higher operation rate compared to large-aperture deflectors and SLMs that makes an advantage in real-time applications. Owing to fast tuning at typical rates above 100 kHz, AOSFs can dramatically extend the performance of dynamic LBS in a number of applications including microparticle manipulation and optical trapping of cold atom ensembles. In particular, they facilitate creating hollow-beam optical traps, which are characterized by reduced heating of the trapped object owing to lower light intensity [41].

One of the methods for increasing the performance of AO devices is application of phased-array piezoelectric transducers for the excitation of ultrasound accompanied by beam steering. Phased-array transducers have been used in AO devices for broadening the operation bandwidth of deflectors and AOTFs [42–46]. In addition, a multi-section piezoelectric transducer can be used for the apodization of acoustic fields and the improvement of the an AOTF's transmission function [47–49]. The effect of a phased-array piezoelectric transducer consists in tilting the wavefront direction of ultrasound and, therefore, changing the Bragg phase-matching conditions between ultrasound and light. There are several techniques for the fabrication of phased-array piezoelectric transducers including the stair-step transducer, proposed by Korpel et al. [26]; the planar π -step array, proposed by Alphonse [50]; and the transducer made of a periodically poled lithium niobate crystal, proposed by Molchanov [44]. If a transducer has several sequential sections emitting ultrasound with different delays, its radiation pattern depends on the ultrasound frequency. In particular, a dual-section piezoelectric transducer with two independent drivers can be used to tilt the effective bulk acoustic wave (BAW) direction in the crystal. The effective wavefront tilt is proportional to the phase delay between radio-frequency (RF) signals applied to the segments of the piezoelectric transducer. Though the effect of BAW beam steering has been known for decades and previously used in a number of AO devices including AOTFs, its application in AOSFs and its effect on the two-dimensional transfer function have not been studied to date.

In this work, we study the application of a phased-array piezoelectric transducer for tuning the two-dimensional transmission function of an AOSF with a noncollinear diffraction geometry. While the standard way to control the AOTF's transfer function is frequency tuning, we propose using phase control and the BAW beam steering phenomenon to tune the AOSF. We present the results of a theoretical analysis and numerical simulations that enable the design of a new AOSF type. A complete analytical model for transfer function simulations is presented and numerical modeling according to this model is performed for an optimized AOSF configuration. The effects of the phase delay between two ultrasonic waves on transformations of the transfer function are described.

2. Theoretical Analysis

A schematic view of a dual-channel AOSF is shown in Figure 1. The piezoelectric transducer is bonded to an AO crystal and has two separate electrodes coated on it. Both electrodes of the piezoelectric transducer have the same length, $L_t/2$ (total effective length of the transducer is L_t). Owing to acoustic anisotropy, there is a walk-off angle ψ between the BAW wave vector and its group velocity vector that causes oblique propagation of the BAW beam. It is assumed that the RF signals applied to the transducer's electrodes have the same frequency f and a relative phase delay $\Delta\phi$. The amplitudes of the RF signals and excited BAWs are equal. Anisotropic AO interaction changes the polarization of the diffracted laser beam from ordinary (o-wave) to extraordinary (e-wave).

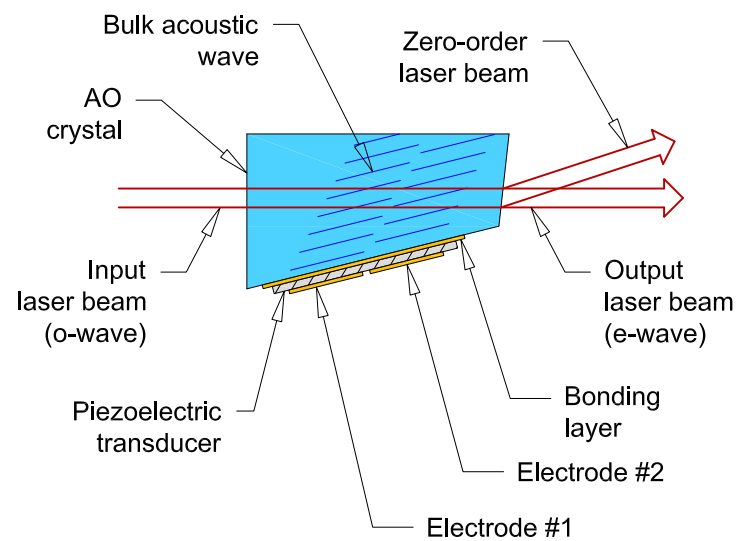


Figure 1. AOFS with a dual piezoelectric transducer: two RF signals are applied to the transducer's electrodes. The laser beam is sequentially diffracted by two BAWs having a relative phase delay of $\Delta\phi$.

The most common AO crystal for the design of AO filters through visible and near-infrared spectral regions is paratellurite (TeO_2). This crystal features a low phase velocity of the slow-shear BAW in the vicinity of the $\langle 110 \rangle$ crystallographic axis, $v \sim 700$ m/s, and high birefringence, $\Delta n/n_o \approx 0.07$. These two factors determine the high diffraction efficiency and good resolution of the filters. In the following numerical simulations in Section 3, we assume paratellurite as the AO crystal for the AOSF. Two main configuration parameters of the filter, which determine its performance, are the crystal cut angle α_0 and the transducer length L_t [39]. The first one determines primary parameters of the AO phase matching, i.e., the ultrasound frequency f and the Bragg angle. The second one affects the performance of key features of the filter, namely, its resolution and diffraction efficiency: both the efficiency and the resolution increase with L_t . Optimization of the AOSF design is based on a trade-off between the efficiency and the resolution that determines the crystal cut angle α_0 [2]. Another feature of paratellurite is strong anisotropy of the BAW properties [51,52]. For this reason, we include the BAW energy walk-off in the numerical simulation model.

For the analytical description of the AO diffraction we use plane-wave one-dimensional coupled-mode equations (CMEs) [53]. Rigorous CME solutions for a periodic acoustic field were previously analyzed by Antonov et al. [45] and by Balakshy et al. [54]. These results include a general-form matrix formalism for computing the performance of a Bragg cell with a multi-element transducer. Hereinafter, we analyze the diffraction of light by two ultrasound layers in an anisotropic crystal, because this configuration can provide efficient acoustic beam steering with a single dual-channel RF driver. Under a nondegenerate Bragg phase-matching condition, only two interacting waves are considered. The complex

amplitudes of the diffraction orders are $C_0(z)$ and $C_1(z)$, respectively. In a homogeneous interaction medium, these amplitudes satisfy Kogelnik’s differential equations [53]

$$\begin{cases} C_0' = -\frac{q}{2}C_1 \exp(-i\eta z - i\Phi); \\ C_1' = \frac{q}{2}C_0 \exp(i\eta z + i\Phi), \end{cases} \tag{1}$$

where q is the coupling coefficient that is proportional to the BAW amplitude, η is the phase mismatch, and Φ is the initial BAW phase. According to the phase-matching theory for anisotropic media developed by Parygin and Chirkov [38], Bragg diffraction is considered as a three-wave mixing process involving two optical waves and the acoustic wave in the crystal. The magnitude of the mismatch η is defined as the projection of the wave vector difference in the direction orthogonal to the BAW group velocity vector. The solution of Equation (1) with initial conditions $C_0(0) = A$ and $C_1(0) = B$ is

$$\begin{cases} C_0(z) = \exp\left(-\frac{i\eta z}{2}\right) \left(A \cos \frac{z\sqrt{q^2 + \eta^2}}{2} + \frac{iA\eta - qB \exp(-i\Phi)}{\sqrt{q^2 + \eta^2}} \sin \frac{z\sqrt{q^2 + \eta^2}}{2} \right); \\ C_1(z) = \exp\left(\frac{i\eta z}{2}\right) \left(B \cos \frac{z\sqrt{q^2 + \eta^2}}{2} - \frac{iB\eta - qA \exp(i\Phi)}{\sqrt{q^2 + \eta^2}} \sin \frac{z\sqrt{q^2 + \eta^2}}{2} \right), \end{cases} \tag{2}$$

where A and B are arbitrary complex amplitudes. According to Equation (2), the BAW phase Φ directly affects the complex amplitudes of both diffraction orders.

Figure 2 illustrates the plane-wave AO interaction model in the region $0 < z < L = L_t \cos \psi$, where ψ is the BAW walk-off angle in the AO crystal. The BAW group velocity vector is orthogonal to the z -axis. As the first step, we take the solution (2) at $z = L/2$ with initial conditions $A = 1$ and $B = 0$, corresponding to only one incident wave:

$$\begin{cases} C_0(L/2) = \exp\left(-\frac{i\eta L}{4}\right) \left(\cos \frac{L\sqrt{q^2 + \eta^2}}{4} + \frac{i\eta}{\sqrt{q^2 + \eta^2}} \sin \frac{L\sqrt{q^2 + \eta^2}}{4} \right); \\ C_1(L/2) = \exp\left(\frac{i\eta L}{4}\right) \frac{q \exp(i\Phi)}{\sqrt{q^2 + \eta^2}} \sin \frac{L\sqrt{q^2 + \eta^2}}{4}. \end{cases} \tag{3}$$

This solution is considered as the initial conditions for the diffraction of light by the second BAW layer, $A = C_0(L/2)$ and $B = C_1(L/2)$, which are substituted into Equation (2). The phase delay is set as

$$\Phi = \frac{\eta L}{2} + \Delta\phi, \tag{4}$$

where the first term is the phase delay owing to the mismatch and $\Delta\phi$ is the preset delay between two BAW signals. The resulting solution for the first diffraction order at the output of two BAW layers is

$$C_1(L) = \exp\left(\frac{i\eta L}{2}\right) \frac{q}{\sqrt{q^2 + \eta^2}} \sin \frac{L\sqrt{q^2 + \eta^2}}{2} \times D(\Delta\phi), \tag{5}$$

where the last factor $D(\Delta\phi)$ includes all terms depending on the phase delay:

$$D(\Delta\phi) = \exp\left(\frac{i\Delta\phi}{2}\right) \left(\cos \frac{\Delta\phi}{2} - \frac{\eta}{\sqrt{q^2 + \eta^2}} \sin \frac{\Delta\phi}{2} \tan \frac{L\sqrt{q^2 + \eta^2}}{4} \right). \tag{6}$$

The case of a uniform transducer with an interaction length of L can be readily derived from Equations (5) and (6), assuming $\Delta\phi = 0$, that obviously results in $D = 1$.

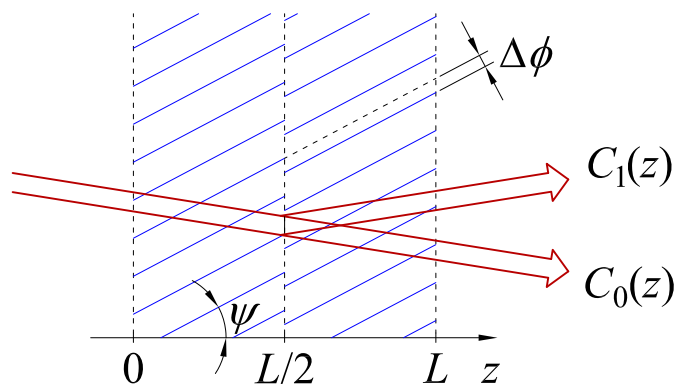


Figure 2. Schematic representation of uniform AO interaction region with two BAWs having the phase delay $\Delta\phi$.

Equation (6) shows that in the case of perfect phase matching ($\eta = 0$), the coupling coefficient q is canceled in the r.h.s. Therefore, for a perfectly phase-matched plane optical wave, the phase delay $\Delta\phi$ between two ultrasonic waves in the AO crystal results only in the decrease in the diffracted beam’s amplitude $C_1(L)$, which is proportional to $\cos(\Delta\phi/2)$.

Since an AO interaction is a linear optical phenomenon, plane-wave decomposition is applicable. Thus, the plane-wave components of the incident and the diffracted beams satisfy CMEs (1), with the phase mismatch η depending on the directional angles θ (Bragg angle) and φ (azimuthal angle). Thus, the field amplitude in the first diffraction order follows Equations (5) and (6). In addition, the phase-matching condition sets an unambiguous relation between the directional angles (θ, φ) for the input beam and corresponding angles (θ_d, φ_d) for the diffracted beam. This relation determines the geometric aberrations of the AOTF, which have been analyzed by Machikhin et al. [55]. In the following analysis, we assume that the input beam is an ordinary wave in a uniaxial crystal, and the diffracted beam is an extraordinary wave.

In the Fourier transform optical scheme proposed by Obydenov et al. for LBS applications [24], the AOSF is placed in the back focal plane of an objective lens. Therefore, the laser beam processed by the filter has a wide angular spectrum and the phase mismatch η cannot be canceled for all plane-wave components of the beam. Thus, the phase mismatch depends on the wave vector of the plane-wave components. As the result, the phase delay $\Delta\phi$ between two BAWs will affect the diffraction efficiency of all angular spectrum components and, therefore, tune the two-dimensional transfer function of the filter.

The intensity transmission function at the first diffraction order is defined as $T_1 = |C_1(L)/C_0(0)|^2$. According to Equation (5) and assuming $C_0(0) = 1$, it can be expressed as

$$T_1(Q, H, \Delta\phi) = \frac{Q^2}{Q^2 + H^2} \sin^2 \frac{\pi}{2} \sqrt{Q^2 + H^2} \times \left(\cos \frac{\Delta\phi}{2} - \frac{H}{\sqrt{Q^2 + H^2}} \sin \frac{\Delta\phi}{2} \tan \frac{\pi}{4} \sqrt{Q^2 + H^2} \right)^2, \quad (7)$$

where $Q = qL/\pi$ and $H = \eta L/\pi$ are the normalized values of the coupling coefficient and the mismatch. Holding other factors constant, Q is proportional to the BAW amplitude. In the experiments on beam shaping, Q and $\Delta\phi$ are the parameters of the RF signal, while H depends on the light propagation direction according to the phase-matching condition.

Figure 3 shows the evolution of $T_1(Q, H)$ with the increase in the phase delay $\Delta\phi$. The first case is $\Delta\phi = 0$, Figure 3a, corresponding to a single transducer having the length of L_t . The last case is $\Delta\phi = \pi$, Figure 3e, corresponding to counter-phase BAW excitation by

the transducer’s segments. In this case, the amplitude of the first sidelobe becomes equal to the amplitude of the main maximum. Analysis of Equation (7) shows that at $\Delta\phi = \pm\pi$, the maximum of $T_1 = 1$ takes place at $H = \mp\sqrt{2}$ and $Q = \sqrt{2}$. In between, the increase in the phase delay has two main effects. Firstly, the value of the mismatch H , at which the maximum of T_1 takes place, is not zero, and its value is proportional to $\Delta\phi$. Secondly, the coupling coefficient Q , providing maximum diffraction efficiency, increases as well.

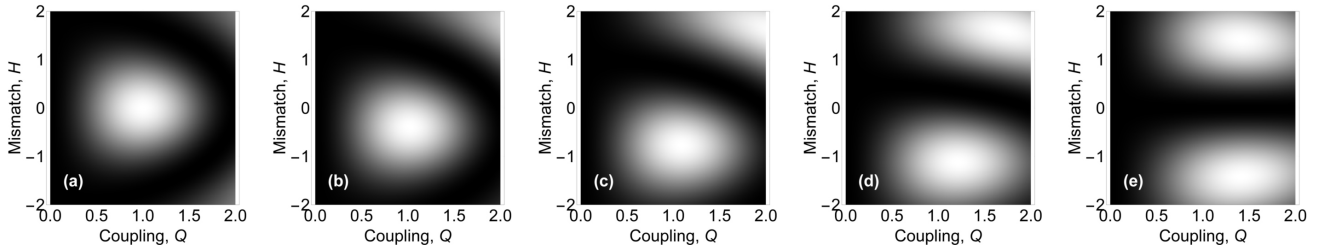


Figure 3. Simulated function $T_1(Q, H, \Delta\phi)$ at various phase delays: (a) $\Delta\phi = 0$; (b) $\Delta\phi = \pi/4$; (c) $\Delta\phi = \pi/2$; (d) $\Delta\phi = 3\pi/4$; and (e) $\Delta\phi = \pi$. Hereinafter, the contour plots use a linear gray level color scheme, with T_1 ranging from 0 (black) to 1 (white).

At perfect phase matching, i.e., $H = 0$ and $\Delta\phi = 0$, maximum diffraction efficiency $T_1 = 1$ occurs when $Q = 1$. This case corresponds to Figure 3a. Figure 4 shows the calculated values of $T_1(1, H, \Delta\phi)$, panel (a), and $T_1(\sqrt{2}, H, \Delta\phi)$, panel (b). In both cases, an almost linear dependence $H(\Delta\phi) = -\Delta\phi/2$ maximizes T_1 over either variable. More accurately, this dependence can be approximated as

$$H_{opt}(\Delta\phi) \approx -0.5\Delta\phi + 0.0038\Delta\phi^3 + 0.00011\Delta\phi^5. \tag{8}$$

With an increase in $\Delta\phi$, the maximum T_1 at $Q = 1$ slightly decreases, which can be compensated by increasing Q . In the case $Q = \sqrt{2}$, there is a strong overcoupling at $\Delta\phi = 0$, resulting in $T_1(\sqrt{2}, 0, 0) \approx 0.63$.

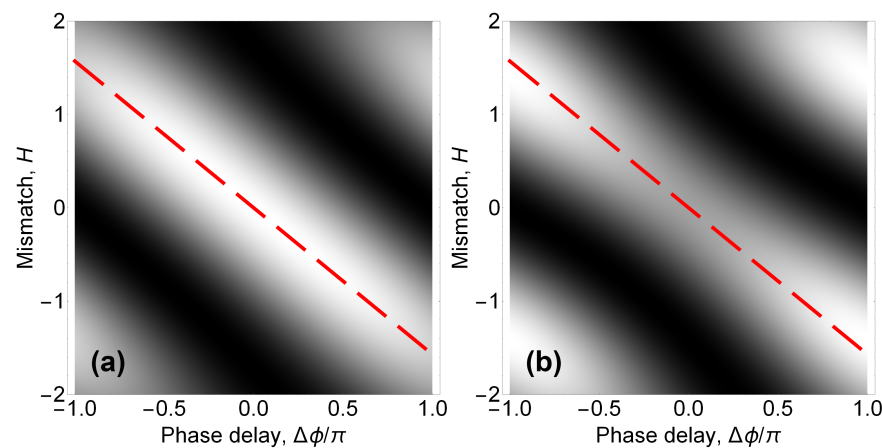


Figure 4. First-order transmission $T_1(Q, H, \Delta\phi)$ as a function of H and $\Delta\phi$: (a) $Q = 1$; (b) $Q = \sqrt{2}$. The color scheme is the same as in Figure 3. Dashed line: linear slope $H = -\Delta\phi/2$.

Figure 5 shows the calculated values of $T_1(Q, -\Delta\phi/2, \Delta\phi)$, i.e., under the assumption of a linear relation between $\Delta\phi$ and H . As follows from this plot, in the whole phase delay range $-1 < \Delta\phi/\pi < 1$, the diffraction efficiency can be above 0.99 if a proper value for the coupling coefficient Q_{opt} is chosen. The optimal value of the coupling coefficient can be numerically approximated with a fourth-order polynomial as follows:

$$Q_{opt}(\Delta\phi) \approx 1 + 0.035\Delta\phi^2 + 0.00069\Delta\phi^4. \tag{9}$$

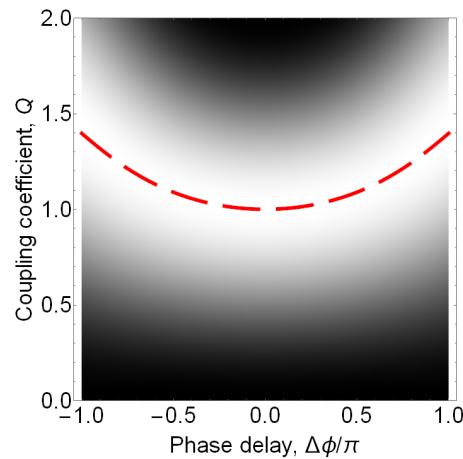


Figure 5. First-order transmission at $H = -\Delta\phi/2$. The color scheme is the same as in Figure 3. Dashed line: optimal coupling coefficient $Q_{opt}(\Delta\phi)$ maximizing T_1 .

However, Equations (8) and (9) are not analytical expressions but only fits to the numerical simulation results. The maximum value $Q = \sqrt{2}$ at $\Delta\phi = \pm\pi$ corresponds to twofold RF driving power compared to the optimal case $Q = 1$ for a uniform transducer.

One can show that the maxima of the diffraction efficiency T_1 are related to the radiation pattern of the phased-array piezoelectric transducer. Calculating the angular spectrum of the acoustic field shown in Figure 2, we derived that the angular position of the main lobe of the radiation pattern is tilted to

$$\Delta\alpha = \frac{0.75v}{\pi f L_t} \Delta\phi, \tag{10}$$

where v is the BAW phase velocity. In the case of the dual-segment transducer, the largest of the sidelobes corresponds to $\Delta\phi \pm 2\pi$, where the “+” sign is for $\Delta\phi < 0$ and vice versa.

The following step of the simulation is to take into account the spatial structure of phase matching. The phase mismatch η has been calculated for a certain diffraction geometry and substituted into Equation (7). Under the condition of anisotropic Bragg diffraction in a uniaxial crystal, which is used in noncollinear AOTFs, it can be written as follows [2]:

$$\eta(\theta, \varphi) = \frac{2\pi}{\lambda} \left\{ n_e(\sin\theta \sin\psi + \cos\theta \cos\varphi \cos\psi) - F \sin\psi - \sqrt{n_o^2 - (n_e \sin\theta - F)^2 - n_e^2 \cos^2\theta + [n_e(\sin\theta \sin\psi + \cos\theta \cos\varphi \cos\psi) - F \sin\psi]^2} \right\}, \tag{11}$$

where $F = f\lambda/v$, n_o is the ordinary refractive index of the AO crystal, and $n_e = n_e(\theta, \varphi)$ is the extraordinary refractive index in the direction of plane-wave propagation. To design an annular spatial frequency filter we choose the NPM diffraction geometry, i.e., the configuration of light and ultrasound propagation directions and frequencies corresponding to the local minimum of $\eta(\theta, \varphi)$. The transfer function of a noncollinear AOSF in this diffraction geometry has the O-type topology, and the radius of the phase-matching locus increases with the ultrasound frequency. Accurate analysis shows that the annular transfer function near the NPM diffraction geometry is slightly asymmetric, and the transfer function center shifts with the ultrasound frequency [2,3].

With respect to Equations (7) and (11), the resulting two-dimensional transfer function will be expressed as $T_1(\theta, \varphi; f, Q, \Delta\phi)$, where θ and φ are the plane-wave direction angles, while f , Q , and $\Delta\phi$ are the problem parameters corresponding to the ultrasound frequency, normalized amplitude, and the phase delay between the transducer sections. These three parameters can be independently controlled in experiments to provide different transfer functions of the AOSF.

3. Results and Discussion

The analytical model developed in Section 2 was applied for numerical simulations of the dual-channel AOSF performance. The transfer function T_1 in Equation (7) is defined in terms of dimensionless parameters. In order to perform the simulations, these parameters were evaluated with respect to a real-life AOSF specification. The coupling coefficient was set to $Q = 1$, and the phase mismatch was computed according to Equation (11).

The simulations were made for a paratellurite AOSF with a cut angle $\alpha_0 = 12.45^\circ$, the transducer length was $L_t = 16$ mm, and the optical wavelength $\lambda = 633$ nm. The BAW parameters for this AOSF configuration are $v = 755$ m/s and $\psi = 56^\circ$. The NPM frequency $f_{npm} = \min f(\theta) = 153.4$ MHz. According to Equation (10), the maximum deviation of the effective crystal cut angle is

$$\Delta\alpha_{max} = \frac{0.75v}{f_{npm}L_t} = 0.013^\circ. \quad (12)$$

Figure 6 shows the transmission coefficient as a function of the Bragg angle θ_d and ultrasound frequency f . The locus of perfect phase-matching points at $\Delta\phi = 0$ is plotted as a dashed line. In panel (a), the dashed line coincides with the maximum $T_1 = 1$. The phase-matching frequency increases with $\Delta\phi$ since the effective crystal cut angle $\alpha = \alpha_0 + \Delta\alpha$ increases linearly. At the same time, the first sidelobe's magnitude increases when $|\Delta\phi| \rightarrow \pi$. Symmetrical splitting of the Bragg curve takes place at $\Delta\phi = \pm\pi$, that is shown in panel (e) and also corresponds to Figure 3e. In the simulated case with only two segments of the transducer used for steering the acoustic beam, the maximum gap between the phase-matching frequencies is 1.6 MHz.

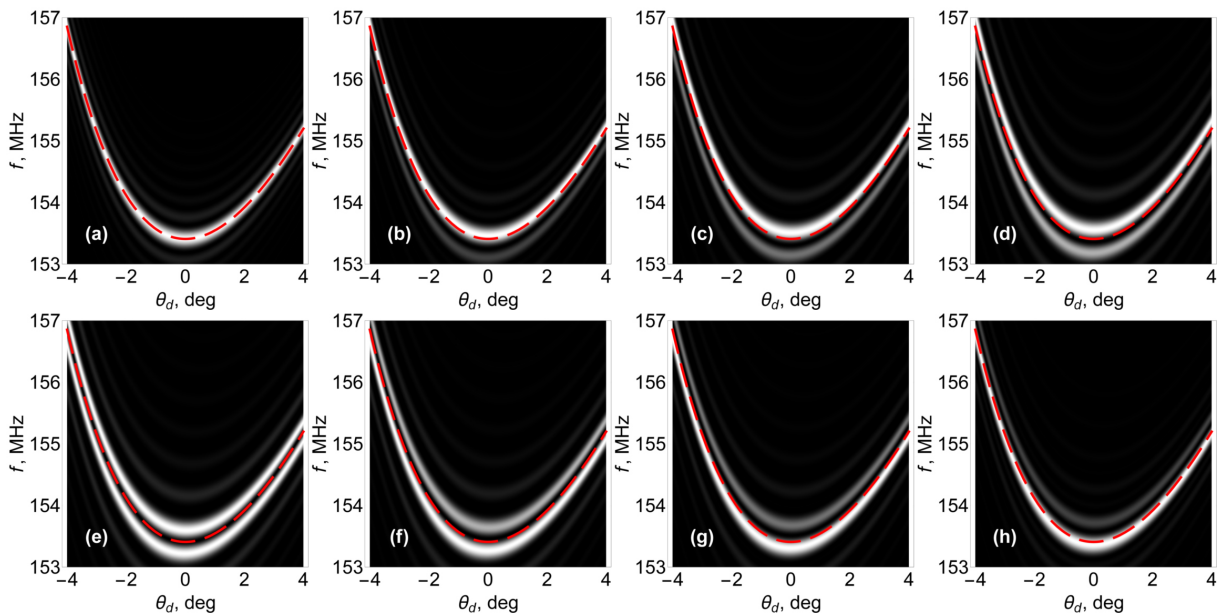


Figure 6. Simulated AOTF transmission $T_1(f, \theta_d)$ in the diffraction plane $\varphi_d = 0$ at various phase delays. Top row: (a) $\Delta\phi = 0$; (b) $\Delta\phi = \pi/4$; (c) $\Delta\phi = \pi/2$; and (d) $\Delta\phi = 3\pi/4$. Bottom row: (e) $\Delta\phi = -\pi$; (f) $\Delta\phi = -3\pi/4$; (g) $\Delta\phi = -\pi/2$; and (h) $\Delta\phi = -\pi/4$. The color scheme is the same as in Figure 3. Dashed line: the Bragg phase-matching dependence $f(\theta_d)$ at $\Delta\phi = 0$.

The following transfer function simulations in Figures 7 and 8 include two cases of the AOSF operational parameters choice. The coupling coefficient $Q = 1$ is fixed in both cases and different ultrasound frequencies f determine the transfer function geometry. Thus, these cases demonstrate two qualitatively different behaviors of the transfer function, which can be achieved in the AOSF using acoustic beam steering.

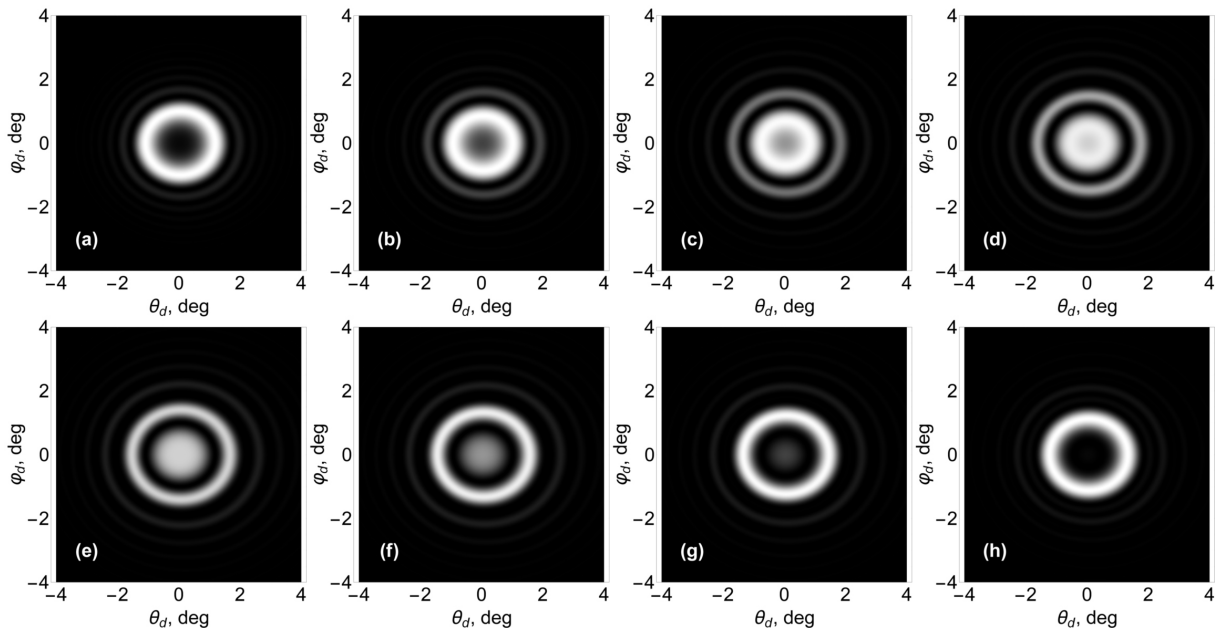


Figure 7. Simulated AOTF two-dimensional transmission function at $f = 153.6$ MHz at various phase delays. Top row: (a) $\Delta\phi = 0$; (b) $\Delta\phi = \pi/4$; (c) $\Delta\phi = \pi/2$; and (d) $\Delta\phi = 3\pi/4$. Bottom row: (e) $\Delta\phi = -\pi$; (f) $\Delta\phi = -3\pi/4$; (g) $\Delta\phi = -\pi/2$; and (h) $\Delta\phi = -\pi/4$. The color scheme is the same as in Figure 3.

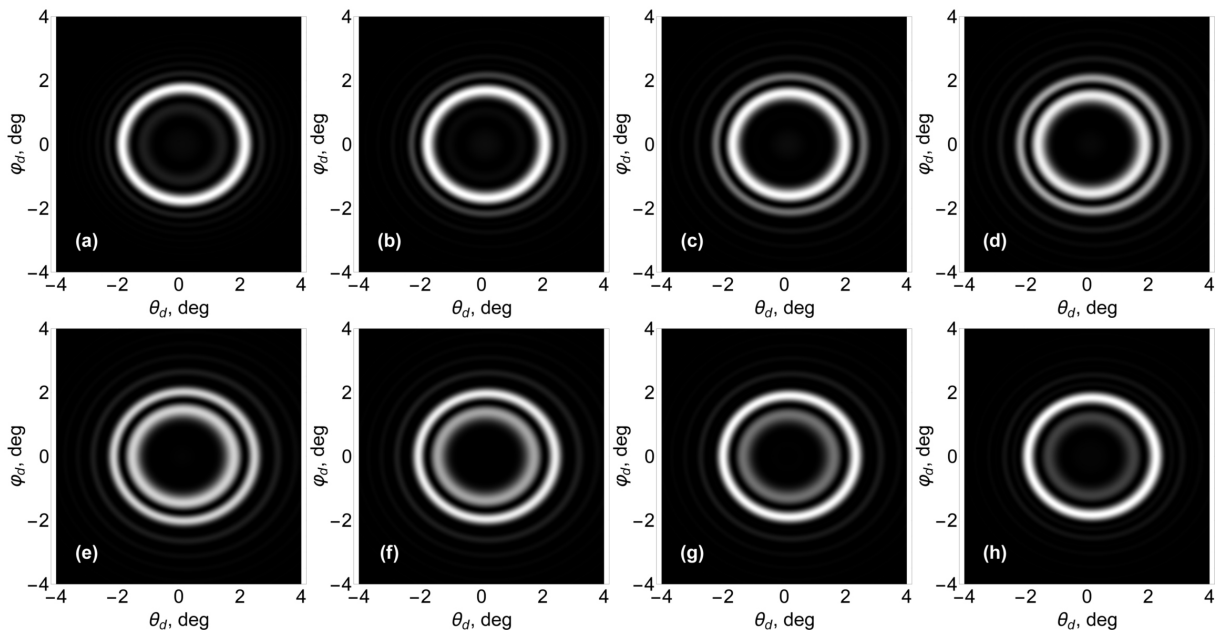


Figure 8. Simulated AOTF two-dimensional transmission function at $f = 154.0$ MHz at various phase delays. Top row: (a) $\Delta\phi = 0$; (b) $\Delta\phi = \pi/4$; (c) $\Delta\phi = \pi/2$; and (d) $\Delta\phi = 3\pi/4$. Bottom row: (e) $\Delta\phi = -\pi$; (f) $\Delta\phi = -3\pi/4$; (g) $\Delta\phi = -\pi/2$; and (h) $\Delta\phi = -\pi/4$. The color scheme is the same as in Figure 3.

The first case in Figure 7 was calculated for $f = 153.6$ MHz. In this case, the NPM condition is satisfied for $\alpha = \alpha_0 + \Delta\alpha_{max}$. The initial annular transfer function is a hollow ring, panel (a), which shrinks into a solid disk with increasing $\Delta\phi$, panels (b)–(d). The transfer function at $\Delta\phi = \pm\pi$, panel (e), is a flat-topped circular region surrounded by a ring. With further increase in the phase delay, the disk vanishes, and the radius of the surrounding ring decreases.

The second case in Figure 8 was calculated for $f = 154.0$ MHz, which is above the NPM frequency for all effective wavefront directions. In this case, even at the maximum tilt of effective wavefronts, panel (e), both phase-matching regions remain rings, while a dark disk remains in the center of the transfer function. The evolution of the transfer function consists in decreasing of the ring radius and transmission coefficient with $\Delta\phi$. Simultaneously, the outer ring of the transfer function is developed, and the corresponding transmission coefficient for this ring increases.

Analyzing Figures 7 and 8, we can observe two main effects of the phase control on the AO transfer function. The first effect dominates at small $\Delta\phi$: when $|\Delta\phi| < \pi/2$ the magnitude of the largest sidelobe is relatively small, and the phase shift results mainly in the variation of the phase matching ring radius (see panels (a), (b), and (h)). In the opposite case, $\pi/2 \leq |\Delta\phi| < \pi$, the effect of the transfer function splitting is the main one (see panels (c)–(g)). Both effects can be purposefully used in AOSF applications. Fine-tuning of the ring radius achieved at small $\Delta\phi$ has an advantage compared to conventional frequency control because the transfer function remains symmetric. Splitting of the transfer functions at larger $\Delta\phi$ provides the same effect as multifrequency control of the AOSF.

4. Summary

Previous experiments with AOSF applications in optical trapping have demonstrated that dynamic reconfiguration of the filter's annular transfer function can be used for effective microparticle manipulation [24]. In those experiments, the AOSF was controlled only by means of frequency tuning. The disadvantage of frequency-only AOSF tuning is the inherent asymmetry of the transfer function [2,3]. The phase control of the transfer function is based on effective acoustic wavefront tilt, which can compensate for this asymmetry of the transfer function. In this report, we demonstrated that tuning of the AOSF's two-dimensional transfer function can be performed using the phase-only RF signal control in a dual-transducer configuration of the filter. The phase delay between the RF signals applied to the piezoelectric transducer's sections changes the phase-matching conditions of anisotropic Bragg diffraction. Two basic operations with the transfer function that can be achieved using phase-only control are changing the radius of the AOSF's annular transfer function and generating a pair of concentric rings separated by a dark region. The experimental validation of the simulation results presented in this paper will be a plot of future work.

The modification of the AOSF's annular transfer function and the possibility of creating dual-ring bottle beams have direct potential applications to optical trapping and microparticle manipulation. Such laser beam configurations can be used in dark optical traps, a type of trap in which resonant particles are repulsed by the laser field and their trapping occurs in the regions with minimum light intensity [41]. With respect to new results in multicolor LBS performed by a single AOSF [25], we foresee further development of this technology for trapping of cold-atom ensembles. The capability dynamic tuning of light distribution by the AOSF at microsecond timescales opens the possibility for advanced experiments with reconfigurable optical traps.

Author Contributions: Conceptualization, K.B.Y. and V.Y.M.; methodology, K.B.Y.; software, A.I.C.; investigation, A.I.C.; writing—original draft preparation, K.B.Y.; writing—review and editing, V.Y.M.; visualization, A.I.C.; project administration, V.Y.M. All authors have read and agreed to the published version of the manuscript.

Funding: This research was funded by the Russian Science Foundation, grant number 20-12-00348 (<https://rscf.ru/en/project/20-12-00348/>, (accessed on 18 October 2023)).

Institutional Review Board Statement: Not applicable.

Informed Consent Statement: Not applicable.

Data Availability Statement: The data presented in this study are available on request from the corresponding author.

Conflicts of Interest: The authors declare no conflict of interest.

Abbreviations

The following abbreviations are used in this manuscript:

AO	Acousto-optic
AOSF	Acousto-optic spatial filter
AOTF	Acousto-optic tunable filter
BAW	Bulk acoustic wave
CME	Coupled-mode equations
LBS	Laser beam shaping
NPM	Noncritical phase matching
RF	Radio-frequency
SLM	Spatial light modulator

References

1. Dickey, F.M. (Ed.) *Laser Beam Shaping: Theory and Techniques*, 2nd ed.; CRC Press: Boca Raton, FL, USA, 2014. [\[CrossRef\]](#)
2. Yushkov, K.B.; Chizhikov, A.I.; Makarov, O.Y.; Molchanov, V.Y. Optimization of noncollinear AOTF design for laser beam shaping. *Appl. Opt.* **2020**, *59*, 8575–8581. [\[CrossRef\]](#) [\[PubMed\]](#)
3. Yushkov, K.B.; Kupreychik, M.I.; Obydenov, D.V.; Molchanov, V.Y. Acousto-optic k-space filtering for multifrequency laser beam shaping. *J. Opt.* **2023**, *25*, 014002. [\[CrossRef\]](#)
4. Balakshy, V.I. Acoustooptical cell as the space frequency filter. *Sov. J. Commun. Technol. Electron.* **1984**, *29*, 1610–1616.
5. Balakshy, V.I.; Kostyuk, D.E. Spatial structure of acousto-optic phase matching in uniaxial crystals. *Opt. Spectr.* **2006**, *101*, 283–289. [\[CrossRef\]](#)
6. Balakshy, V.I.; Kostyuk, D.E. Acousto-optic image processing. *Appl. Opt.* **2009**, *48*, C24–C32. [\[CrossRef\]](#) [\[PubMed\]](#)
7. Kotov, V.M.; Averin, S.V.; Kotov, E.V.; Shkerdin, G.N. Acousto-optic filters based on the superposition of diffraction fields. *Appl. Opt.* **2018**, *57*, C83–C92. [\[CrossRef\]](#)
8. Gorevoy, A.V.; Machikhin, A.S.; Martynov, G.N.; Pozhar, V.E. Spatiospectral transformation of noncollimated light beams diffracted by ultrasound in birefringent crystals. *Photonics Res.* **2021**, *9*, 687–693. [\[CrossRef\]](#)
9. Kupreychik, M.I.; Yushkov, K.B. Topological evolution of acousto-optic transfer functions in biaxial crystals. *J. Opt. Soc. Am. B* **2022**, *39*, 3169–3177. [\[CrossRef\]](#)
10. Yushkov, K.B.; Naumenko, N.F. Optical beam diffraction tensor in birefringent crystals. *J. Opt.* **2021**, *60*, 095602. [\[CrossRef\]](#)
11. Lu, G.; Fei, B. Medical hyperspectral imaging: A review. *J. Biomed. Opt.* **2014**, *19*, 010901. [\[CrossRef\]](#)
12. Korablev, O.I.; Belyaev, D.A.; Dobrolenskiy, Y.S.; Trokhimovskiy, A.Y.; Kalinnikov, Y.K. Acousto-optic tunable filter spectrometers in space missions. *Appl. Opt.* **2018**, *57*, C103–C119. [\[CrossRef\]](#) [\[PubMed\]](#)
13. Banerjee, P.P.; Cao, D.; Poon, T.-C. Basic image-processing operations by use of acousto-optics. *Appl. Opt.* **1997**, *36*, 3086–3089. [\[CrossRef\]](#) [\[PubMed\]](#)
14. Cao, D.; Banerjee, P.P.; Poon, T.-C. Image edge enhancement with two cascaded acousto-optic cells with contrapropagating sound. *Appl. Opt.* **1998**, *37*, 3007–3014. [\[CrossRef\]](#) [\[PubMed\]](#)
15. Banerjee, P.P.; Cao, D.; Poon, T.-C. Notch spatial filtering with an acousto-optic modulator. *Appl. Opt.* **1998**, *37*, 7532–7537. [\[CrossRef\]](#)
16. Voloshinov, V.B.; Babkina, T.M.; Molchanov, V.Y. Two-dimensional selection of optical spatial frequencies by acousto-optic methods. *Opt. Eng.* **2002**, *41*, 1273–1280. [\[CrossRef\]](#)
17. Balakshy, V.I.; Voloshinov, V.B. Acousto-optic image processing in coherent light. *Quantum Electron.* **2005**, *35*, 85–90. [\[CrossRef\]](#)
18. Yushkov, K.B.; Molchanov, V.Y.; Belousov, P.V.; Abrosimov, A.Y. Contrast enhancement in microscopy of human thyroid tumors by means of acousto-optic adaptive spatial filtering. *J. Biomed. Opt.* **2016**, *21*, 016003. [\[CrossRef\]](#)
19. Kotov, V.M.; Averin, S.V.; Zenkina, A.A.; Belousova, A.S. Two-dimensional image processing using two channels formed by one acousto-optical filter. *Comput. Opt.* **2023**, *46*, 905–913. [\[CrossRef\]](#)
20. Wang, P.; Fan, H.; Zhang, Y.; Yao, Y.; Zhang, B.; Qin, W.; Poon, T.-C. Isotropic two-dimensional differentiation based on dual dynamic volume holograms. *Photonics* **2023**, *10*, 828. [\[CrossRef\]](#)
21. Balakshy, V.I. Acousto-optic visualization of optical wavefronts. *Appl. Opt.* **2018**, *57*, C56–C63. [\[CrossRef\]](#)
22. Machikhin, A.S.; Burmak, L.; Polschikova, O.V.; Ramazanov, A.G.; Pozhar, V.E.; Boritko, S.V. Multispectral phase imaging based on acousto-optic filtration of interfering light beams. *Appl. Opt.* **2018**, *57*, C64–C69. [\[CrossRef\]](#) [\[PubMed\]](#)
23. Yushkov, K.B.; Champagne, J.; Kastelik, J.-C.; Makarov, O.Y.; Molchanov, V.Y. AOTF-based hyperspectral imaging phase microscopy. *Biomed. Opt. Express* **2020**, *11*, 7053–7061. [\[CrossRef\]](#) [\[PubMed\]](#)
24. Obydenov, D.V.; Yushkov, K.B.; Molchanov, V.Y. Ring-shaped optical trap based on acousto-optic tunable spatial filter. *Opt. Lett.* **2021**, *46*, 4494–4497. [\[CrossRef\]](#) [\[PubMed\]](#)
25. Obydenov, D.V.; Yushkov, K.B.; Molchanov, V.Y. Independent multicolored bottle beam generation using acousto-optic spatial shaping of a femtosecond laser beam. *Opt. Lett.* **2023**, *48*, 5320–5323. [\[CrossRef\]](#) [\[PubMed\]](#)

26. Korpel, A.; Adler, R.; Desmares, P.; Watson, W. Direct observation of optically induced generation and amplification of sound. *Appl. Opt.* **1966**, *5*, 1667–1675. [[CrossRef](#)]
27. Hilaire, P.S.; Benton, S.A.; Lucente, M. Synthetic aperture holography: A novel approach to three-dimensional displays. *J. Opt. Soc. Am. A* **1992**, *9*, 1969–1977. [[CrossRef](#)]
28. Gulyaev, Y.V.; Kazaryan, M.A.; Mokrushin, Y.M.; Shakin, O.V. Acousto-optic laser projection systems for displaying TV information. *Quantum Electron.* **2015**, *45*, 283–300. [[CrossRef](#)]
29. Treptow, D.; Bola, R.; Martín-Badosa, E.; Montes-Usategui, M. Artifact-free holographic light shaping through moving acousto-optic holograms. *Sci. Rep.* **2021**, *11*, 21261. [[CrossRef](#)]
30. Antonov, S.N.; Rezvov, Y.G. Efficient multi-beam Bragg acoustooptic diffraction with phase optimization of a multifrequency acoustic wave. *Tech. Phys.* **2007**, *52*, 1053–1060. [[CrossRef](#)]
31. Antonov, S.N.; Vainer, A.V.; Proklov, V.V.; Rezvov, Y.G. Highly effective acoustooptic diffraction of light by multifrequency sound using a nonaxial deflector. *Tech. Phys.* **2008**, *53*, 752–756. [[CrossRef](#)]
32. Trypogeorgos, D.; Harte, T.; Bonnin, A.; Foot, C. Precise shaping of laser light by an acousto-optic deflector. *Opt. Express* **2013**, *21*, 24837–24846. [[CrossRef](#)] [[PubMed](#)]
33. Szulzycki, K.; Savaryn, V.; Grulkowski, I. Generation of dynamic Bessel beams and dynamic bottle beams using acousto-optic effect. *Opt. Express* **2016**, *24*, 23977–23991. [[CrossRef](#)] [[PubMed](#)]
34. Szulzycki, K.; Savaryn, V.; Grulkowski, I. Rapid acousto-optic focus tuning for improvement of imaging performance in confocal microscopy. *Appl. Opt.* **2018**, *57*, C14–C18. [[CrossRef](#)] [[PubMed](#)]
35. Karimi, Y.; Scopelliti, M.G.; Do, N.; Alam, M.-R.; Chamanzar, M. In situ 3D reconfigurable ultrasonically sculpted optical beam paths. *Opt. Express* **2019**, *27*, 7249–7265. [[CrossRef](#)]
36. Bola, R.; Treptow, D.; Marzoa, A.; Montes-Usategui, M.; Martín-Badosa, E. Acousto-holographic optical tweezers. *Opt. Lett.* **2020**, *45*, 2938–2941. [[CrossRef](#)]
37. Dixon, R.W. Acoustic diffraction of light in anisotropic media. *IEEE J. Quantum Electron.* **1967**, *3*, 85–93. [[CrossRef](#)]
38. Parygin, V.N.; Chirkov, L.E. Diffraction of light by ultrasound in an anisotropic medium. *Sov. J. Quantum Electron.* **1975**, *5*, 180–184. [[CrossRef](#)]
39. Gottlieb, M. Acousto-optic tunable filters. In *Design and Fabrication of Acousto-Optic Devices*; Goutzoulis, A., Pape, D., Eds.; Marcel Dekker: New York, NY, USA, 1994; Chapter 4, pp. 197–284.
40. Mazur, M.M.; Suddenok, Y.A.; Shorin, V.N. Double acousto-optic monochromator of images with tunable width of the transmission function. *Tech. Phys. Lett.* **2014**, *40*, 167–169. [[CrossRef](#)]
41. Ashkin, A. History of optical trapping and manipulation of small-neutral particle, atoms, and molecules. *IEEE J. Sel. Top. Quantum Electron.* **2000**, *6*, 841–856. [[CrossRef](#)]
42. Coquin, G.A.; Griffin, J.P.; Anderson, L.K. Wide band acoustooptic deflectors using acoustic beam steering. *IEEE Trans. Son. Ultrason.* **1970**, *17*, 34–40. [[CrossRef](#)]
43. Chang, I.C. Wideband bragg cell techniques. *Proc. SPIE* **1987**, *789*, 105–110. [[CrossRef](#)]
44. Molchanov, V.Y. Acousto-optic TeO₂ devices using regular domain structure transducers. *Acta Phys. Slovaca* **1996**, *46*, 715–720.
45. Antonov, S.N.; Vainer, A.V.; Proklov, V.V.; Rezvov, Y.G. Extension of the angular scanning range of the acousto-optic deflector with a two-element phased-array piezoelectric transducer. *Tech. Phys.* **2013**, *58*, 1346–1351. [[CrossRef](#)]
46. Balakshy, V.; Kupreychik, M.; Mantsevich, S.; Molchanov, V. Acousto-optic cells with phased-array transducers and their application in systems of optical information processing. *Materials* **2021**, *14*, 451. [[CrossRef](#)]
47. Chang, I.C. Acousto-optic tunable filters. *Opt. Eng.* **1981**, *20*, 824–829. [[CrossRef](#)]
48. Pieper, R.; Korpel, A.; Hereman, W. Extension of the acousto-optic Bragg regime through Hamming apodization of the sound field. *J. Opt. Soc. Am. A* **1986**, *3*, 1608–1619. [[CrossRef](#)]
49. Vanhamel, J.; Dupont, S.; Kastelik, J.-C.; Dekemper, E. Design of a radio frequency compensation system, using the electrical characterisation of a multitransducer acousto-optical tunable filter. In Proceedings of the Forum Acusticum 2023, Torino, Italy, 11–15 September 2023; p. 349.
50. Alphonse, G.A. Broadband acoustooptic deflectors: New results. *Appl. Opt.* **1975**, *14*, 201–207. [[CrossRef](#)]
51. Uchida, N.; Ohmachi, Y. Elastic and photoelastic properties of TeO₂ single crystal. *J. Appl. Phys.* **1970**, *40*, 4692–4695. [[CrossRef](#)]
52. Balakshy, V.I.; Mantsevich, S.N. Propagation of acoustic beams in a paratellurite crystal. *Acoust. Phys.* **2012**, *58*, 549–557. [[CrossRef](#)]
53. Yariv, A.; Yeh, P. *Optical Waves in Crystals*; Wiley: New York, NY, USA, 1984.
54. Balakshy, V.I.; Kupreychik, M.I.; Mantsevich, S.N. Light Diffraction on Ultrasound in a Spatially Periodic Acoustic Field. *Opt. Spectrosc.* **2019**, *127*, 712–718. [[CrossRef](#)]
55. Machikhin, A.; Batshev, V.; Pozhar, V.E. Aberration analysis of AOTF-based spectral imaging systems. *J. Opt. Soc. Am. A* **2017**, *34*, 1109–1113. [[CrossRef](#)] [[PubMed](#)]

Disclaimer/Publisher’s Note: The statements, opinions and data contained in all publications are solely those of the individual author(s) and contributor(s) and not of MDPI and/or the editor(s). MDPI and/or the editor(s) disclaim responsibility for any injury to people or property resulting from any ideas, methods, instructions or products referred to in the content.